arXiv:1410.6357v2 [physics.flu-dyn] 18 Feb 2015

Spermatozoa scattering by a microchannel feature: an elastohydrodynamic model

T. D. Montenegro-Johnson[1,2,3]*; H. Gadêlha[4,3] and D. J. Smith[2,3,5].

[1] Department of Applied Mathematics and Theoretical Physics, Centre for Mathematical Sciences, University of Cambridge, Wilberforce Road, Cambridge, CB3 0WA, U.K.

[2] School of Mathematics, University of Birmingham, Edgbaston, Birmingham, B15 2TT, U.K.

[3] Centre for Human Reproductive Science, Birmingham Women's NHS Foundation Trust, Mindelsohn Way, Edgbaston, Birmingham, B15 2TG, U.K.

[4] Wolfson Centre for Mathematical Biology, University of Oxford, Mathematical Institute, Woodstock Road, OX2 6GG, U.K.

[5] School of Engineering and Centre for Scientific Computing, University of Warwick, Coventry, CV4 7AL, U.K.

Abstract

Sperm traverse their microenvironment through viscous fluid by propagating flagellar waves; the waveform emerges as a consequence of elastic structure, internal active moments, and low Reynolds number fluid dynamics. Engineered microchannels have recently been proposed as a method of sorting and manipulating motile cells; the interaction of cells with these artificial environments therefore warrants investigation. A numerical method is presented for large-amplitude elastohydrodynamic interaction of active swimmers with domain features. This method is employed to examine hydrodynamic scattering by a model microchannel backstep feature. Scattering is shown to depend on backstep height and the relative strength of viscous and elastic forces in the flagellum. In a 'high viscosity' parameter regime corresponding to human sperm in cervical mucus analogue, this hydrodynamic contribution to scattering is comparable in magnitude to recent data on contact effects, being of the order of 5–10°. Scattering can be positive or negative depending on the relative strength of viscous and elastic effects, emphasising the importance of viscosity on the interaction of sperm with their microenvironment. The modulation of scattering angle by viscosity is associated with variations in flagellar asymmetry induced by the elastohydrodynamic interaction with the boundary feature.

Key index words: *Stokesian swimming, fluid-structure interaction, human sperm*

*Author for correspondence, email: tdj23@cam.ac.uk

1 Introduction

Human sperm propel themselves by propagating a travelling wave along a single, active flagellum; this motility is essential for migration through the female reproductive tract and natural fertilisation. Recent work with microfluidic devices [1, 2] has suggested the ability to direct and sort cells through their own motility, a potentially valuable advance in assisted reproduction therapy and in the livestock industry. Cell scattering at simple geometric features, such as the outside of a corner, appear to be dependent on viscosity and temperature; developing mechanical models to understand, interpret and optimise these effects for their exploitation is therefore of considerable interest. We will develop a mathematical model of a cell interacting with its environment, and its computational implementation, and study the dynamics of a realistic model sperm swimming over a backstep feature to study the effect of elastic, viscous and geometric parameters. The model will combine geometric nonlinearity of the elastic flagellum with nonlocal hydrodynamic interactions, and will be solved numerically via an implicit finite difference method for the elastohydrodynamic equations, combined with a hybrid slender body theory/boundary integral method for the low Reynolds number fluid dynamics.

The motor apparatus driving the flagellar waveform is a remarkably phylogenetically conserved structure known as the axoneme. The axoneme in human sperm comprises 9 doublet microtubules, linked to each other and a central pair by passive elastic structures, with additional stiffening from outer dense fibres and the fibrous sheath (for recent review focused on mechanically-relevant features, see ref. [3]). Motor proteins bound to microtubules exert forces on adjacent doublets in a coordinated manner to induce bending moments along the length of the flagellum, causing bending, which is in turn resisted by the surrounding fluid. The fluid mediates interactions with surrounding surfaces and other cells; the flagellar waveform emerges from this nonlinear coupling.

Machin [4] showed that in order to generate experimentally observed waveforms, the flagellum must actively bend along its length, developing a linearised theory that has formed the basis of many subsequent studies. The theory that bending is produced by relative sliding of internal microtubules was subsequently proposed by Satir [5], and the sliding mechanism was modelled in early studies by Brokaw [6, 7], using the formalism of an active internal moment per unit length in an elastic filament. The regulation of the active motor proteins that cause this sliding, and their oscillatory behaviour, is however a subject of continuing enquiry [8, 9, 10], with modelling playing an important role in comparing regulatory theories [11]. A number of studies since the 1970s have provided significant insights into how potential mechanisms of dynein regulation can produce the types of bending waves observed in nature (see for example [12, 13, 14, 15, 8]).

The importance of large-amplitude elastohydrodynamic flagellar modelling was established by Gadêlha et al. [16], who delineated the range of validity of small-amplitude elastic theory and showed that for sufficiently high viscosity relative to flagellar stiffness, a buckling instability can give rise to waveform asymmetry without domain boundaries or asymmetric internal actuation. The numerical implementation of Gadêlha et al.'s study built on a model of passive flexible fibres in shear flow [17], although replacing the nonlocal hydrodynamics of the latter with a local drag-velocity law. The combination of three-dimensional, time-dependent flow with the hydrodynamic interactions arising from fixed and moving boundaries, with active filament mechanics is computationally demanding; the majority of sperm models until the last decade made similar approximations for the fluid dynamics, or small-amplitude linearisation of the flagellar wave.

Liron, Gueron and colleagues (see for example [18, 19]) modelled cilia arrays, taking both

nonlocal fluid dynamics and geometric nonlinearity into account, building on earlier work by for example Lighthill [20] and Hines & Blum [13]. However this formalism, expressed in terms of bending angles rather than flagellar position, does not appear to have been generalised to a free-swimming cell with the associated boundary condition resulting from the presence of a head. More recent work using the finite element and finite volume methods and cluster computing has also been focused on cilia [21]; another successful recent approach is the regularised stokeslet method combined with a generalised immersed boundary method [22].

While the fluid dynamic interaction of sperm with plane boundaries has received significant attention since the work of Rothschild over 50 years ago [23], motivating a number of experimental and theoretical studies [24, 25, 26, 27], the interaction of sperm with 'non-trivial' geometric obstacles involving angles and curves or complex interfaces is a subject of growing recent interest [28, 29, 30, 31].

Denissenko et al. [1] showed how sperm scatter at a range of angles when encountering the outside of a corner in an artificial microchannel maze, and that the scattering angle is modulated by viscosity; Kantsler et al. [2] studied the effect of very close interactions of sperm and the biflagellate algae *Chlamydomonas* with these features. The geometric nature of the female reproductive tract is also highly convoluted, further motivating the need for models which can accommodated complex wall shapes into account. These studies suggest tantalising opportunities to direct and sort motile sperm on passive microdevices, however a better understanding of the subtle nonlinear physics of how flagellated swimmers interact with geometric features must be developed; to aid with this understanding we will develop a mathematical and computational approach which accounts for elasticity, viscosity and their interaction, without the need for large scale computational resources. To this end we will bring together the active elastic formulation of Gadêlha *et al.* [16] with the Lighthill-Gueron-Liron theorem [18] for nonlocal slender body theory and the boundary element [32] and regularised stokeslet methods [33, 34] to capture the influence of a non-trivial nearby surface. We will use this approach to explore how sperm scatter near geometric features due to elastohydrodynamic interaction over hundreds of flagellar beats with a single computer core, and quantify how the balance of viscosity and elasticity modulates this effect via changes to the flagellar waveform.

2 Mathematical model

The mathematical model of a sperm interacting with a geometric feature will be derived from, (i) the Stokes flow equations, with a nonlocal hydrodynamic model, and (ii) geometrically nonlinear elasticity for an internally actuated flagellum. We will first derive the equations for the two parts of problem, before describing (iii) the numerical implementation.

2.1 Hydrodynamics

At microscopic scales, fluid dynamics can be modelled by the incompressible Stokes flow equations,

$$0 = -\boldsymbol{\nabla} p + \mu \nabla^2 \mathbf{u}, \quad \boldsymbol{\nabla} \cdot \mathbf{u} = 0, \tag{1}$$

where $\mathbf{u}$ is velocity, p is pressure and μ is dynamic viscosity. For our problem, these equations will be augmented with the no-slip, no-penetration condition $\mathbf{u}(\mathbf{X}) = \mathbf{X}_t$ for points $\mathbf{X}$ on the solid boundary, where subscript t denotes time derivative.

The linearity of the Stokes flow equations enables the construction of solutions to satisfy boundary conditions via discrete and/or continuous sums of suitably-weighted fundamental

solutions. These techniques replace solid surfaces, such as the sperm flagellum, head, and its surrounding microenvironment, by line or surface distributions of immersed forces. A concentrated point force located at $\mathbf{y}$ with strength $\mathbf{F}$, produces a velocity field (the 'stokeslet'),

$$u_j(\mathbf{x}) = S_{jk}(\mathbf{x},\mathbf{y})F_k, \quad \text{where} \quad S_{jk}(\mathbf{x},\mathbf{y}) = \frac{1}{8\pi\mu}\left(\frac{\delta_{jk}}{|\mathbf{x}-\mathbf{y}|} + \frac{(x_j-y_j)(x_k-y_k)}{|\mathbf{x}-\mathbf{y}|^3}\right), \tag{2}$$

the symbol δ_{jk} being the Kronecker delta tensor and the summation convention being used. The symbol $\mathsf{S}(\mathbf{x},\mathbf{y})$ will be used to denote the 2nd rank tensor in equation (2). It will also be convenient to make use of the regularised stokeslet S^ϵ of Cortez [35], which corresponds to a spatially smoothed force; a frequently-used implementation in three dimensions [33] takes the form,

$$S^\epsilon_{jk}(\mathbf{x},\mathbf{y}) = \frac{1}{8\pi\mu}\frac{\delta_{jk}(|\mathbf{x}-\mathbf{y}|^2+2\epsilon^2)+(x_j-y_j)(x_k-y_k)}{(|\mathbf{x}-\mathbf{y}|^2+\epsilon^2)^{3/2}}. \tag{3}$$

The parameter $\epsilon > 0$ defines the length scale over which the point force is smoothed; this smoothness property is particularly convenient for the formulation of boundary integral methods.

The LGL theorem [19], an extension of the work of Lighthill [20], derives from a line distribution of singular stokeslets and source dipoles: an approximate expression for the flow field at the surface of a moving slender body, accurate to $O(\sqrt{b/L})$, where b is the radius and L is the flagellar length. Ignoring image systems, which are not required in our formulation, and using the properties of the stokeslet to reorder the source and field points, we have the expression for the approximate velocity field produced by the slender body $\mathbf{v}$,

$$\begin{aligned}\mathbf{v}(\mathbf{X}(s_0,t)) = &-\frac{1}{\xi_\parallel}(\mathbf{f}_{\text{vis}}\cdot\hat{\mathbf{s}})\hat{\mathbf{s}} - \frac{1}{\xi_\perp}(\mathbf{f}_{\text{vis}}\cdot\hat{\mathbf{n}})\hat{\mathbf{n}} - \frac{1}{\xi_\perp}(\mathbf{f}_{\text{vis}}\cdot\hat{\mathbf{b}})\hat{\mathbf{b}} \\ &- \int_{|s-s_0|>q} \mathsf{S}(\mathbf{X}(s_0,t),\mathbf{X}(s,t))\cdot\mathbf{f}_{\text{vis}}(s)\,ds.\end{aligned} \tag{4}$$

Here and in what follows, $0 \leqslant s \leqslant L$ is an arclength parameterisation for the flagellum, and $\mathbf{f}_{\text{vis}}$ is the viscous force per unit length exerted by the fluid on the flagellum. The coefficients $\xi_\parallel$ and $\xi_\perp$ are parallel and perpendicular resistance coefficients similar to those of Gray & Hancock [36] and take the form,

$$\xi_\perp = \frac{8\pi\mu}{1+2\ln(2q/b)}, \quad \xi_\parallel = \frac{8\pi\mu}{-2+4\ln(2q/b)}, \quad \gamma = \frac{\xi_\perp}{\xi_\parallel}, \tag{5}$$

the parameter q being a length scale chosen intermediate in magnitude between b and L. The symbols $\hat{\mathbf{s}}$, $\hat{\mathbf{n}}$ and $\hat{\mathbf{b}}$ are unit tangent, normal and binormal. Whereas Gueron and Liron [18, 19] considered the dynamics of a cilium projecting from a plane boundary, and hence the associated image systems, in this study we will not require these terms because surfaces will be represented via boundary integrals.

Equation (4) can be considered a nonlocal extension of resistive force theories, which retain only the first three terms. To couple LGL to the elastohydrodynamic model of Gadêlha et al. [16] we will rewrite these terms in another commonly-used form, $-(1/\xi_\perp)(\mathbf{I}+(\gamma-1)\hat{\mathbf{s}}\hat{\mathbf{s}})\cdot\mathbf{f}_{\text{vis}}$, with $\gamma = \xi_\perp/\xi_\parallel$ playing a similar role to the drag anisotropy ratio of resistive force theory, but depending on the choice of q. The precise value of q is not critical provided that $b \ll q \ll L$ because changes to the resistance coefficients are accompanied by changes to the integrals; for our study with $b = 0.01L$, we choose $q = 0.1L$, leading to $\gamma \approx 1.4$.

To model a sperm, we will consider a cell with a rigid head as well as a flagellum, swimming near a rigid step-like surface. The linearity of Stokes flow equations means that

a solution satisfying the additional no-slip boundary conditions associated with the head and the wall may be constructed by linear superposition. Moreover, the Lorentz reciprocal relation, and its regularised analogue [33] enable the representation of these surfaces by boundary integrals; rigidity of the surfaces enables the use of single layer boundary integral representations [37, p. 32]. In the present study we will use a hybrid approach, representing the head via a surface distribution of singular stokeslets with stress $\boldsymbol{\phi}^{\mathrm{H}}$, discretised via BEMLIB [32], and the wall by regularised stokeslets and boundary elements, with stress $\boldsymbol{\phi}^{\mathrm{W}}$ [33, 34]. The full fluid dynamic model for the velocity field on the surface of the flagellum is therefore,

$$\begin{aligned}\mathbf{u}(\mathbf{X}(s_0,t)) = -\frac{1}{\xi_\perp}(\mathbf{I}+(\gamma-1)\hat{\mathbf{s}}\hat{\mathbf{s}})\cdot\mathbf{f}_{\mathrm{vis}} - \int_{|s-s_0|>q}\mathbf{S}(\mathbf{X}(s_0,t),\mathbf{X}(s,t))\cdot\mathbf{f}_{\mathrm{vis}}(s)\,ds \\ - \iint_{H(t)}\mathbf{S}(\mathbf{X}(s_0,t),\mathbf{y})\cdot\boldsymbol{\phi}^{\mathrm{H}}(\mathbf{y})\,dS_{\mathbf{y}} - \iint_{W}\mathbf{S}^{\epsilon}(\mathbf{y},\mathbf{X}(s_0,t))\cdot\boldsymbol{\phi}^{\mathrm{W}}(\mathbf{y})\,dS_{\mathbf{y}}. \qquad (6)\end{aligned}$$

Similar equations, but with the first two terms replaced by a single slender body integral $-\int_0^L \mathbf{S}\cdot\mathbf{f}_{\mathrm{vis}}\,ds$, hold on the surface of the head and the wall. In the next section we will discuss the equations of an internally-driven elastic flagellum, and their coupling to the fluid mechanics.

2.2 Elastohydrodynamics

The elastohydrodynamic formulation we will work with was derived by Tornberg & Shelley [17], and extended to an internally-driven flagellum by Gadêlha et al. [16]; the central feature of this approach is to formulate the problem in terms of the flagellar position $\mathbf{X}(s,t)$ and line tension $T(s,t)$. Alternative approaches based on bending angles and curvatures [38, 39] have also been pursued, as has complex curvature [40]. The internal elastic contact force $\mathbf{F}_{\mathrm{int}}$ and moment $\mathbf{M}_{\mathrm{int}}$ exerted on the proximal flagellum $[0,s_0)$ by the distal flagellum (s_0,L), respectively are given by,

$$\mathbf{F}_{\mathrm{int}} = -E\mathbf{X}_{sss} + m\hat{\mathbf{n}} + T\mathbf{X}_s, \quad \mathbf{M}_{\mathrm{int}}\wedge\mathbf{X}_s = E\mathbf{X}_{ss}, \qquad (7)$$

where E is constant elastic modulus and $m(s,t)$ is a prescribed active moment density representing the internal flagellar motors. Balancing elastic and viscous forces acting on a segment of flagellum $(s_0, s_0+\delta s)$ and taking the limit as $\delta s\to 0$ yields,

$$\mathbf{f}_{\mathrm{vis}} + \partial_s(-E\mathbf{X}_{sss} + m\hat{\mathbf{n}} + T\mathbf{X}_s) = 0. \qquad (8)$$

Noting that $\hat{\mathbf{s}} = \mathbf{X}_s$, the local term of equation (6) can then be written,

$$\begin{aligned}-\frac{1}{\xi_\perp}(\mathbf{I}+(\gamma-1)\hat{\mathbf{s}}\hat{\mathbf{s}})\cdot\mathbf{f}_{\mathrm{vis}} = -E(\mathbf{X}_{ssss} + (\gamma-1)(\mathbf{X}_s\cdot\mathbf{X}_{ssss})\mathbf{X}_s) + T\mathbf{X}_{ss} + \gamma T_s\mathbf{X}_s \\ + m_s\hat{\mathbf{n}} + \gamma m\hat{\mathbf{n}}_s. \qquad (9)\end{aligned}$$

For brevity we will write the nonlocal (integral) velocities from equation (6) as $\mathbf{V}$ (written out explicitly in the appendix, equation (18)). Nondimensionalising with scales L for position, $1/\omega$ for time, ωL for velocity and E/L^2 for tension and moment density, yields the following dimensionless elastohydrodynamic equation,

$$\mathrm{Sp}^4(\mathbf{X}_t - \mathbf{V}) = -\mathbf{X}_{ssss} - (\gamma-1)(\mathbf{X}_s\cdot\mathbf{X}_{ssss})\mathbf{X}_s + T\mathbf{X}_{ss} + \gamma T_s\mathbf{X}_s + m_s\hat{\mathbf{n}} + \gamma m\hat{\mathbf{n}}_s. \qquad (10)$$

The parameter $\mathrm{Sp} = L(\xi_\perp \omega/E)^{1/4}$ is the *sperm number*, which quantifies the relative importance of viscous and elastic effects. This model can be seen as an extension of linear models (such as Camalet et al. [14]) by the inclusion of the nonlinear terms on the right hand side, and an extension of hydrodynamically local models (such as Gadêlha et al. [16]) by the inclusion of the $\mathbf{V}$ term on the left hand side.

Similarly to Gadêlha et al. [16], the inextensibility constraint $\partial_t(\mathbf{X}_s \cdot \mathbf{X}_s) = 0$ can be used with the elastohydrodynamic equation (10) to deduce an ordinary differential equation which must be satisfied by the line tension T,

$$\begin{aligned} -\mathrm{Sp}^4 \mathbf{V}_s \cdot \mathbf{X}_s = \gamma T_{ss} - \mathbf{X}_{ss} \cdot \mathbf{X}_{ss} T + 3\gamma \mathbf{X}_{sss} \cdot \mathbf{X}_{sss} + (1+3\gamma)\mathbf{X}_{ss} \cdot \mathbf{X}_{ssss} \\ + (\gamma+1) m_s \hat{\mathbf{n}}_s \cdot \mathbf{X}_s + m \hat{\mathbf{n}}_{ss} \cdot \mathbf{X}_s. \end{aligned} \tag{11}$$

The above equation is derived via the identity $3\mathbf{X}_{ss} \cdot \mathbf{X}_{sss} + \mathbf{X}_s \cdot \mathbf{X}_{ssss} = 0$ and its derivative with respect to s. As previously [17, 16] we introduce the term $\lambda \mathrm{Sp}^4(1 - \mathbf{X}_s \cdot \mathbf{X}_s)$ to the left hand side of equation (11) to dampen numerical errors in flagellar length. The value used in the present study is $\lambda = 80$, though as found by Gadêlha *et al.* the solution is insensitive to the precise value of λ.

The final part of the mathematical model is the specification of the boundary conditions for equations (10) and (11). The assumption of zero contact force and moment at the distal ($s = 1$) tip of the flagellum combined with the elasticity equations (7) yield (in dimensionless variables),

$$0 = -\mathbf{X}_{sss} + m\hat{\mathbf{n}} + T\mathbf{X}_s, \quad 0 = \mathbf{X}_{ss} \quad \text{at } s = 1. \tag{12}$$

Taking the dot product of the first equation with $\mathbf{X}_s$, using the identity $\mathbf{X}_s \cdot \mathbf{X}_{sss} = -\mathbf{X}_{ss} \cdot \mathbf{X}_{ss}$ and the second equation yields the distal tension boundary condition, $T = 0$.

At the proximal end of the flagellum, the boundary conditions are given by considering the force and moment exerted by the fluid on the head. We denote these quantities $\mathbf{F}^{\mathrm{H}}$ and $\mathbf{M}^{\mathrm{H}}$ and nondimensionalise them with the elastic scalings E/L^2 and E/L respectively. In the inertialess Stokes flow regime, the total force and moment acting on the head are zero, so by Newton's third law, the force and moment on the flagellum at $s = 0$ are also given by $\mathbf{F}^{\mathrm{H}}$ and $\mathbf{M}^{\mathrm{H}}$ respectively. With the appropriate scalings, the proximal boundary conditions are then,

$$\mathbf{F}^{\mathrm{H}} = \mathbf{X}_{sss} - m\hat{\mathbf{n}} - T\mathbf{X}_s \quad \text{and} \quad \mathbf{M}^{\mathrm{H}} \wedge \mathbf{X}_s = -\mathbf{X}_{ss} + M\hat{\mathbf{n}}, \quad \text{at } s = 0, \tag{13}$$

where $M = \int_0^1 m\, ds$. From these equations we also derive the tension condition at the proximal end, $\mathbf{F}^{\mathrm{H}} \cdot \mathbf{X}_s = -\mathbf{X}_{ss} \cdot \mathbf{X}_{ss} - T$. The calculation of the quantities $\mathbf{F}^{\mathrm{H}}$ and $\mathbf{M}^{\mathbf{H}}$ with nonlocal hydrodynamic interaction is described in more detail in the next section and the appendix. Finally we introduce the translational and angular velocity $\mathbf{U}^{\mathrm{H}}$ and $\mathbf{\Omega}^{\mathrm{H}}$ of the head; while $\mathbf{U}^{\mathrm{H}}$ and two components of the angular velocity are constrained by knowledge of the function $\mathbf{X}$, there is an independent rotational component of the motion that defines the principal bending plane of the flagellum. These quantities will be determined by kinematic considerations and the implementation of the boundary conditions.

To complete the mathematical model it is necessary to specify the internal active moment $m(s,t)$. Gadêlha et al. [16] used travelling waves of internal moment, which calculations from experiment [3] confirm are a good model. We therefore specify in dimensionless units, $m(s,t) = m_0 \cos(ks - t)$.

2.3 Numerical implementation

The elastohydrodynamic equation (10) is treated with a Crank-Nicolson type finite difference discretisation, with the second order central differences in the interior, and third order

one-sided difference for the boundary conditions, using coefficients taken from Fornberg [41]. The higher-order boundary stencil produced comparable errors to the central stencil on polynomial test functions. Both linear and nonlinear terms are treated implicitly; nonlinearity of these equations is dealt with by performing an iterative process on every timestep, with the operator on the left hand side at $t + dt$ being linearised as,

$$-\mathbf{X}_{ssss} - (\gamma - 1)(\tilde{\mathbf{X}}_s \cdot \mathbf{X}_{ssss})\tilde{\mathbf{X}}_s + T\tilde{\mathbf{X}}_{ss} + \gamma T_s \tilde{\mathbf{X}}_s + m_s \tilde{\mathbf{n}} + \gamma m \tilde{\mathbf{n}}_s, \tag{14}$$

variables with tildes denoting that values from the previous iteration are taken.

The nonlocal hydrodynamic term $\mathbf{V}$ in equation (10) is approximated by forming the slender body/boundary integral problem of determining $\mathbf{f}_{\text{vis}}$, $\boldsymbol{\phi}^{\text{H}}$ and $\boldsymbol{\phi}^{\text{W}}$ using the most recent approximations to $\tilde{\mathbf{X}}$ and $\tilde{\mathbf{X}}_t$ available; details are given in the appendix.

At the first iteration of each timestep the converged values from the previous timestep are used as starting guesses for all variables, except for $\mathbf{X}$ which is approximated via linear extrapolation. The nonlinear iteration is terminated when the maximum difference in position between successive iterations relative to the distance travelled by the flagellum over the timestep falls below 0.5%. Similarly, the auxiliary equation for the tension at $t + dt$ is linearised as,

$$\begin{aligned}\mathrm{Sp}^4(\lambda(1 - \tilde{\mathbf{X}}_s \cdot \mathbf{X}_s) - \tilde{\mathbf{V}}_s \cdot \tilde{\mathbf{X}}_s) = \gamma T_{ss} - (\tilde{\mathbf{X}}_{ss} \cdot \tilde{\mathbf{X}}_{ss})T + 3\gamma \tilde{\mathbf{X}}_{sss} \cdot \mathbf{X}_{sss} + (1 + 3\gamma)\tilde{\mathbf{X}}_{ss} \cdot \mathbf{X}_{ssss} \\ + (\gamma + 1)(\tilde{\mathbf{n}}_s \cdot \tilde{\mathbf{X}}_s)m_s + (\tilde{\mathbf{n}}_{ss} \cdot \tilde{\mathbf{X}}_s)m.\end{aligned} \tag{15}$$

Each iteration requires the solution of a linear system for the unknown discrete values of $\mathbf{X}(s_l, t_{n+1})$, $T(s_l, t_{n+1})$, $\mathbf{U}^{\text{H}}$ and $\boldsymbol{\Omega}^{\text{H}}$, where $l = 0, \ldots, N_s$ denotes the spatial grid coordinate and $n = 0, 1, \ldots$ the timestep. We found that $N_s = 160$ and 200 time steps per beat were sufficient to yield accurate results. The discrete form of equations (10) and (11) provide $4(N_s+1)+6 = 650$ linear equations, the additional 6 equations arising from the translational and angular velocity of the cell head. The nonlinear correction is then a system of $3(N_s + N_h + N_b)$ linear equations, where N_h and N_b are the number of elements on the head and domain boundary respectively.

To implement the boundary conditions (12), (13), the force and moment on the head are *a priori* unknown and need to be determined as part of the coupled problem. The force and moment are decomposed into a linear part, given by the grand resistance matrix associated with rigid body motion in the vicinity of the wall, and an additional subleading correction resulting from the influence of the flagellum. Following nondimensionalisation with the elasticity scalings, the force and moment on the head may then be expressed as,

$$\begin{pmatrix}\mathbf{F}^{\text{H}} \\ \mathbf{M}^{\text{H}}\end{pmatrix} = \mathrm{Sp}^4\left(\frac{\mu}{\xi_\perp}\right)\mathcal{R} \cdot \begin{pmatrix}\mathbf{U}^{\text{H}} \\ \boldsymbol{\Omega}^{\text{H}}\end{pmatrix} + \begin{pmatrix}\Delta\mathbf{F}^{\text{H}} \\ \Delta\mathbf{M}^{\text{H}}\end{pmatrix}, \tag{16}$$

where $\Delta\mathbf{F}^{\text{H}}$, $\Delta\mathbf{M}^{\text{H}}$ are corrections for the effect of the flagellum. The calculations of $\mathcal{R}$ and the corrections are described in the appendix.

In summary, each timestep requires a number of iterations to solve the nonlinear problem and each iteration involves the solution of a sparse linear system arising from the finite difference discretisation of the elastohydrodynamic equations. The 'right hand side' terms arising from the nonlocal hydrodynamic correction $\mathbf{V}$ and the nonlocal corrections to the force and moment balance $\Delta\mathbf{F}^{\text{H}}$, $\Delta\boldsymbol{\Omega}^{\text{H}}$ require the solution of a slender body theory-boundary integral hydrodynamic problem. Calculation of the grand resistance matrix $\mathcal{R}$ requires the separate solution of a boundary integral problem with multiple right hand sides to determine the force and moment resistances associated with the rigid body modes of the head and the wall

interaction. The code is implemented in Fortran 90 (gfortran, GNU Compiler Collection); linear systems are equilibriated and solved by LU factorisation with the LAPACK routines `dgeequ` and `dgesv` respectively, and the boundary integrals over the sperm head are calculated with routines from BEMLIB [32]. A typical run of 200 beats with 500 boundary elements required approximately 24 hours walltime on a single core of a 2.2 GHz Intel Sandy Bridge E5-2660 node.

3 Results

The numerical scheme is applied to predict the trajectory of a sperm-like cell swimming in an unbounded fluid at varying Sp, over a 'backstep' (the latter being shown in figure 1a), the limiting case of zero backstep height being referred to as a 'strip'. As in Gadêlha et al. [16], we consider planar waveform actuation, which is appropriate for cells swimming through high viscosity fluids such as cervical mucus [42]. The semi-axes of the ellipsoidal head, modelled with the boundary element method, are $a_x = 0.05L$, $a_y = 0.03L$, $a_z = 0.04L$, which correspond to $5 \times 3 \times 4\,\mu m$ for a flagellum of length $L = 50$ μm. The swimmer is initially at rest, with a straight flagellum, and a 'soft start' is applied whereby the internal shear moment is initially low and smoothly increases to its maximum, reaching 99% after 5 beats. The sperm number of a human gamete can be approximated by using bending stiffness $E \approx 5 \times 10^{-21}$ Nm^2, beat frequency 10–20 Hz giving an angular frequency $\omega \approx 100$ rad/s [3]. Taking a flagellar radius of 0.5 μm, viscosity $\mu \approx 0.14$ Pa·s (similar to mucus analogue [42]) yields the normal resistance coefficient $\xi_\perp \approx 0.503$ and sperm number Sp ≈ 15.8. Therefore, we will consider a range of sperm numbers between 13 and 17, fixing the magnitude of the internally generated shear-force $m_0 = 240$ and wavenumber $k = 6\pi$. The resulting waveforms are shown in figure 1(a). As sperm number increases, beat amplitude is suppressed, as is observed for sperm in high viscosity medium [42], leading to a reduction in side-to-side yaw. All simulations in infinite fluid, i.e. with no nearby boundaries, produced trajectories which were straight overall, once the within-beat yaw was accounted for (data submitted to DRYAD repository [43]); flagellar waveforms for Sp = 13, 15 and 17 are shown in figure 1(b,c).

Figure 2 shows a planar projection of the trajectories $(X(0,t), Y(0,t))$, and the tangent angle $\theta := \arctan(dY/dX(s=0))$ (in degrees) of those trajectories, of cells swimming over backsteps of varying height. The derivative dY/dX is calculated numerically by sampling the trajectory at the temporal midpoint of each beat-cycle and taking centred differences. Colour indicates the trajectory over the backstep of the height in figure 2(a, c, e) with green denoting $h = 0$ and red denoting $h = 0.5$. Simulations were performed over backsteps of height $h = 0.05, 0.1, \ldots, 0.5$, and are displayed up to the time at which $X(0,t) \geqslant 1$.

The results in figure 2(a, c, e) suggest that the backstep affects swimmers at different sperm numbers differently, producing a range of scattering angles. However, it is important in these results to factor out the effects of the strip from the backstep. Taking the (lightest) green trajectory, representing a strip, as a baseline comparison, it is evident that for all sperm numbers the hydrodynamic effect of the backstep is to deflect the swimmer downwards relative to a strip trajectory. Figure 2(b, d, f) reveal that this downward deflection is not smooth, rather there is a sharp bump at $x = 0$ where the head initially passes over the backstep, and a further bump at around $x = 0.3$ where the effect of the step itself becomes subleading relative to boundary interactions between the head and the lower wall.

Simulations were also performed comparing the effect of the backstep to a 'cliff' geometry, with the lower portion of the backstep missing (data submitted [43]). After passing the backstep, cells swam straight as though in an infinite fluid, suggesting that the majority of

the angular deflection occurs due to interaction with the lower boundary; boundary forces change suddenly over a step jump, and the cell acts as though it were above a higher boundary. Additionally, simulations over a strip at Sp = 13 for different starting heights (data submitted [43]) showed that attraction to the surface initially increased and then decreased as height above the surface increased, which suggests that hydrodynamic boundary attraction is responsible for the behaviour in figure 2(a, b).

Figure 3 shows the effect of varying sperm number over finer increments for backstep height zero (a, b) and $h = 0.2L$ (c, d), with results summarised in figure 4(a). Simulations were performed for $\mathrm{Sp} = 13, 13.5, \ldots, 17$ over both a strip geometry and a backstep of height $h = 0.2L$, so that the sperm cells initially start $0.2L$ above the surface, and then increase to around $0.4L$ after the backstep. In figure 3(a–d), colour is matched to increasing sperm number, so that light green corresponds to Sp = 13 and red to Sp = 17. Figure 3(a, b) show for a sperm swimming over a strip, the boundary repels the swimmer more at this close distance as sperm number is increased. This effect is to be expected because increasing the sperm number increases the relative strength of viscous to elastic forces, thus the effect of the boundary is likely to be enhanced as Sp increases. The initial dip in figure 3(b) is an artifact of the numerical soft start of our system, as the waveform emerges from a straight initial state.

Figure 3(c, d) show a larger range of scattering angles than for fixed sperm number over various backstep heights, of the order of 10°. Furthermore, additional simulations (data submitted [43]) showed that this hydrodynamic deflection was not sensitive to the phase of the waveform as it passed over the backstep, in contrast to scattering due to contact forces (R. Goldstein, personal communication, 2014). Figure 4(a) shows the effects of changing sperm number, giving the deflection for a strip, a backstep, and their difference. A slight increase in the magnitude of this difference is observed as sperm number is increased, owing to increased hydrodynamic interaction mediated by viscosity.

Figure 4(b) summarises the effect of varying both backstep height and sperm number simultaneously, quantified by the 'final deflection angle' θ_d, i.e. the value of θ for which $X = L$. At Sp = 13 deflection is always negative, whereas for Sp = 15, 17 deflection is always positive. The relationship between θ_d and h is non-monotone at the lower sperm number but is monotonic in the higher range. At Sp = 13, the deflection angle initially increases in magnitude, then decreases after the maximum at around $h = 0.15L$. This riser height corresponds to a distance of $0.35L$ between the cell and the boundary, which is where boundary attraction is strongest at this sperm number. For Sp = 15, 17 the deflection angle decreases monotonically with backstep height in the range we have considered. This effect likely occurs because at these sperm numbers, the strip causes the cell to pitch away. However in all cases increasing backstep height to $0.5L$ results in a plateau.

The effects of the backstep on the waveform are summarised in figure 5, which show the waveform shape with and without the boundary, and quantitative measures of the asymmetry of the waveform. Recall that the flagellar actuation is symmetric; waveform asymmetry is produced due to increased hydrodynamic drag arising from proximity to the wall [44] affecting closer portions of the flagellum more than further portions. Figure 5(a) shows waveforms at sperm number Sp = 13, 17 in infinite fluid as well as over a strip. In infinite fluid, the waveform is symmetrical for all sperm numbers considered, while the presence of a boundary gives rise to a waveform asymmetry that increases with Sp.

'Asymmetry' is quantified by sampling the flagellar wave every 41 numerical timesteps (relative to a beat cycle of 200 timesteps), projecting into the body frame, and calculating the average lateral position relative to the body frame centreline over a fixed period, in this case beats 82–90. This quantity is plotted as a function of arclength in figure 5(b); its distal

($s = 1$) value is plotted in figure 5(c).

Figure 5(b) plots asymmetry versus arclength for sperm numbers in the range 13–17, the effect being largest at higher sperm number. The asymmetry at the tip of the flagellum for a strip versus no boundary is shown in figure 5(c) as a function of sperm number.

4 Discussion

A numerical method for simulating the swimming of monoflagellate cells over geometric features was presented and applied to model sperm interacting with microchannel backstep feature. The scheme incorporates nonlocal hydrodynamics with large-amplitude active filament mechanics. We believe this method to be the simplest generalisation of previous work that is capable of taking into account nonlocal hydrodynamic interaction geometrical features. The linearity of the Stokes flow equations entails that the largest error in our method arises from the LGL slender body theory, which is at worst on the order of the square root of the slenderness ratio. Accuracy of the method of regularised stokeslets is on the order of the regularisation parameter near the boundary, and its square far from the boundary where the swimmer is located. Future work may consider boundary integral modelling of the flagellum also, however we do not expect that this would qualitatively change swimmer trajectories.

The interaction between the cell and the lower boundary involves the competing effects of asymmetric hydrodynamic forces leading to waveform asymmetry and boundary repulsion, and the pitching behaviour associated with swimmer/boundary interaction [26]. At lower sperm number and at greater distances from the boundary, waveform asymmetry is smaller, and the cell pitches towards the boundary. At higher sperm number and closer distances from the boundary, waveform asymmetry is larger and the cell pitches away. The effect of the backstep is a sudden drop in the lower boundary, which changes the relative importance of these effects; waveform asymmetry is reduced relative to hydrodynamic attraction, and the net result is a deflection towards the lower boundary after the backstep relative to the expected trajectory over a strip (figure 2).

Analysing sperm scattering over a backstep, we found that hydrodynamic effects may be comparable in magnitude in the relatively high viscosity range considered to the contact interactions found experimentally by Kantsler et al. [2]. A transition is predicted from scattering towards the backstep at lower viscosity to scattering away from the backstep at higher viscosity. Qualitatively this behaviour is similar to the temperature-related transition in Kantsler et al.'s observations (with lower temperature corresponding to higher viscosity); the correspondence is not exact however, with Kantsler et al.'s observations being carried out with bull sperm in low viscosity buffer, and with cells exhibiting very close interaction with the boundary, compared with our longer range interactions and sperm number representative of human cells in mucus analogue that we chose to focus on in the present study. Clearly integrating both surface interactions and hydrodynamics will be necessary to develop a comprehensive model, particularly at higher sperm number/viscosity.

The role of hydrodynamic interactions in determining surface attraction and more complex effects associated with boundary features continues to receive significant theoretical attention and is stimulating novel mathematical approaches [28, 29, 45, 30, 31]. Viscous interactions of course become increasingly important in high viscosity fluids such as mucus and laboratory analogues. Kantsler et al. [2] noted the need to take both elastic and steric interactions into account; modelling very short length scale or contact interactions, with either glass, epithelium, cumulus, or even ciliated surfaces, and their effect on the flagellar wave, is a topic of importance, though numerical simulation requires taking account of the rapidly

varying hydrodynamic force and electrostatic interactions as the swimmer approaches these boundaries. We hope that the numerically implicit method, potentially also combined with adaptive refinement of the boundary element meshes, will enable accurately resolved simulation of sperm-like swimmers in very near surface-contact in future work. Other valuable methods for modelling three-dimensional sperm motility and elastic-fluid interaction include models based exclusively on regularised stokeslets [46, 47] and techniques such as stochastic rotation dynamics [48].

Whilst we have used our model to examine a swimmer representative of human sperm, the approach is applicable to a much wider range of eukaryotic cells, including the sperm of other species and, with a slight reworking of the head boundary condition, biflagellate organisms such as the green alga *Chlamydomonas*. These species are of particular interest as they have been used as models for flagellar synchronisation [49] and are relevant to energy-producing bioreactors [50]. For these systems, the model may also be extended to include a nonlocal hydrodynamic contribution from other swimmers. Larger swimming organisms, such as *C. elegans*, have also been shown to be significantly affected by interactions with a structured microenvironment [51, 52].

Another application are is the design and optimisation of biomimetic artificial microswimmers (see for example refs. [53, 54]). Because the model includes internal periodic actuation via prescribed bending moments, it might be used to optimise actuation for various purposes such as forward progress, subject to constraints such as fixed mechanical energy. Furthermore, the inclusion of geometrical boundary features and the use of sperm number allows such optimisation to be tailored to specific environments. The elastohydrodynamic model can additionally be used to solve the inverse problem of estimating internal moments from observed flagellar data, potentially allowing us to examine how nature has optimised swimming in various environments and informing truly biomimetic design.

Despite the linearity of the Stokes flow equations, the interaction of sperm with their microenvironment presents a subtle nonlinear mechanics problem. Sperm scattering depends nonlinearly on the ratio between viscous and elastic forces, with even a simple backstep feature producing attractive or repulsive scattering of cells depending on parameter values. These scattering effects may be valuable in sorting cells in microdevices, in addition to giving insight into the complexity of how sperm interact with their microenvironment. The combination of mechanical models and experiment will provide the best way to understand and exploit these effects for biomedical applications.

Data accessibility

Trajectory and waveform data supporting the findings in this paper have been submitted to DRYAD; see reference item [43].

Competing interests

None.

Authors' contributions

TDMJ designed the research, implemented algorithms, analysed results and co-wrote the manuscript. HG designed the research and contributed to the writing of the manuscript.

DJS designed the research, helped with algorithmic implementation, co-wrote the manuscript and supervised the project.

Acknowledgements

The authors thank Dr Eamonn Gaffney (University of Oxford), Prof. Ray Goldstein (University of Cambridge), Dr Vasily Kantsler, Dr Petr Denissenko (University of Warwick), Prof. John Blake (University of Birmingham) and Dr Jackson Kirkman-Brown (University of Birmingham/Birmingham Women's NHS Foundation Trust) for continuing valuable discussions.

Funding

This work was supported by EPSRC grant EP/K007637/1 to DJS, supporting TDMJ. TDMJ is supported by a Royal Commission for the Exhibition of 1851 Research Fellowship. HG acknowledges a Hooke Fellowship held at the University of Oxford. The computations described in this paper were performed using the University of Birmingham's BlueBEAR HPC service, which was purchased through SRIF-3 funds. See http://www.bear.bham.ac.uk for more details.

Appendix: calculation of hydrodynamic terms

Following nondimensionalisation, the hydrodynamic model yields the following equation for the dimensionless fluid velocity away from the flagellum,

$$\mathrm{Sp}^4\mathbf{U}(\mathbf{x}) = \frac{\xi_\perp}{\mu}\left(\int_0^1 \mathsf{S}(\mathbf{x},\mathbf{X}(s,t))\cdot\mathbf{f}_{\mathrm{vis}}(s,t)ds + \iint_{H(t)} \mathsf{S}(\mathbf{x},\mathbf{Y})\cdot\boldsymbol{\phi}^{\mathrm{H}}(\mathbf{Y},t)dS_{\mathbf{Y}} + \iint_W \mathsf{S}^\epsilon(\mathbf{x},\mathbf{Y})\cdot\boldsymbol{\phi}^{\mathrm{W}}(\mathbf{Y},t)dS_{\mathbf{Y}}\right). \tag{17}$$

The nonlocal contribution to the velocity $\mathbf{V}$ on the slender body is similarly given by,

$$\mathrm{Sp}^4\mathbf{V}(\mathbf{X}(s_0,t)) = \frac{\xi_\perp}{\mu}\left(\int_{|s-s_0|>q} \mathsf{S}(\mathbf{X}(s_0,t),\mathbf{X}(s,t))\cdot\mathbf{f}_{\mathrm{vis}}(s,t)ds + \iint_{H(t)} \mathsf{S}(\mathbf{X}(s_0,t),\mathbf{Y})\cdot\boldsymbol{\phi}^{\mathrm{H}}(\mathbf{Y},t)dS_{\mathbf{Y}} + \iint_W \mathsf{S}^\epsilon(\mathbf{X}(s_0,t),\mathbf{Y})\cdot\boldsymbol{\phi}^{\mathrm{W}}(\mathbf{Y},t)dS_{\mathbf{Y}}\right). \tag{18}$$

At each step of the iterative solution to the nonlinear problem, the collocation code solves the integral equation,

$$\mathrm{Sp}^4\begin{pmatrix}\mathbf{X}_t\\ \mathbf{U}^{\mathrm{H}}+\boldsymbol{\Omega}^{\mathrm{H}}\wedge(\mathbf{Y}^{\mathrm{H}}-\mathbf{X}^{\mathrm{c}})\\ 0\end{pmatrix} = \begin{pmatrix}-(\mathsf{I}+(\gamma-1)\hat{\mathbf{s}}\hat{\mathbf{s}})\cdot\mathbf{f}_{\mathrm{vis}}+\mathrm{Sp}^4\mathbf{V}[\mathbf{f}_{\mathrm{vis}},\boldsymbol{\phi}^{\mathrm{H}},\boldsymbol{\phi}^{\mathrm{W}}](\mathbf{X})\\ \mathrm{Sp}^4\mathbf{U}[\mathbf{f}_{\mathrm{vis}},\boldsymbol{\phi}^{\mathrm{H}},\boldsymbol{\phi}^{\mathrm{W}}](\mathbf{Y}^{\mathrm{H}})\\ \mathrm{Sp}^4\mathbf{U}[\mathbf{f}_{\mathrm{vis}},\boldsymbol{\phi}^{\mathrm{H}},\boldsymbol{\phi}^{\mathrm{W}}](\mathbf{Y}^{\mathrm{W}})\end{pmatrix}, \tag{19}$$

for the unknown hydrodynamic force per unit length $\mathbf{f}_{\mathrm{vis}}$ and unknown stresses $\boldsymbol{\phi}^{\mathrm{H}}$, $\boldsymbol{\phi}^{\mathrm{W}}$.

The collocation code discretises the flagellum with 160 elements, with the nonlocal contribution to the LGL slender body theory computed by the midpoint rule with constant

force per unit length over each element. The force per unit area on the ellipsoidal head of 32 mesh elements is calculated using routines from BEMLIB [32] with 20 point Gauss-Legendre quadrature as described in detail in the appendix. The wall boundary is discretised into elements of width $0.075L$, using regularised stokeslets with $\epsilon = 0.01L$. Integration is performed with repeated Gauss-Legendre quadrature with 4×4 points per element for the near-singular wall integrals, and a 2×2 point rule elsewhere.

To implement the boundary conditions (12), (13), Gadêlha et al. [16] approximated the force and moment on the head by a grand resistance matrix [32] multiplying the velocity and angular velocity. In dimensional variables, the grand resistance matrix expresses the force and moment on a moving rigid body as

$$\begin{pmatrix} \mathbf{F} \\ \mathbf{M} \end{pmatrix} = \mathcal{R} \cdot \begin{pmatrix} \mathbf{U} \\ \mathbf{\Omega} \end{pmatrix}, \quad \text{where} \quad \mathcal{R} = \begin{pmatrix} \mathcal{R}^{\mathrm{F}} \\ \mathcal{R}^{\mathrm{M}} \end{pmatrix}.$$

The blocks $\mathcal{R}^{\mathrm{F}}$ and $\mathcal{R}^{\mathrm{M}}$ are 3×6 matrices yielding the force and moment terms respectively. For example, a sphere of radius a in the absence of hydrodynamic interactions would have dimensionless grand resistance matrix given by

$$\mathcal{R}^{\mathrm{F}} = \begin{pmatrix} -6\pi\mu a \mathbf{I} & 0 \end{pmatrix}, \quad \mathcal{R}^{\mathrm{M}} = \begin{pmatrix} 0 & -8\pi\mu a^3 \mathbf{I} \end{pmatrix}. \tag{20}$$

This approach is convenient because the linearity of the relationship means that the head velocity $\mathbf{U}^{\mathrm{H}}$ and angular velocity $\mathbf{\Omega}^{\mathrm{H}}$ can be dealt with in the implicit formulation as unknowns in the linear algebra problem. To generalise to a nonlocal hydrodynamic model taking into account the effect of the flagellum and nearby boundary, the force and moment will be decomposed as consisting of part which is linear in velocity and angular velocity via resistance matrices and a remaining contribution from the flagellum. The matrices $\mathcal{R}^{\mathrm{F}}$ and $\mathcal{R}^{\mathrm{M}}$ are determined via the boundary integral method, taking into account the potentially highly significant effect of the wall feature, but not the subleading effect of the flagellum, which is accounted for as a correction, as described below.

Elastic scalings are used to nondimensionalise all forces and moments, i.e. $E/L^2, E/L$ for $\mathbf{F}^{\mathrm{H}}$ and $\mathbf{M}^{\mathrm{H}}$ respectively, with E/L^3 for force per unit length $\mathbf{f}_{\mathrm{vis}}$ and E/L^4 for stress $\boldsymbol{\phi}^{\mathrm{H}}, \boldsymbol{\phi}^{\mathrm{W}}$. The additional corrections $\Delta\mathbf{F}^{\mathrm{H}}$ and $\Delta\boldsymbol{M}^{\mathrm{H}}$ referred to in equation (16) are determined as part of the iterative process by performing a slender body/boundary integral calculation of $\tilde{\mathbf{f}}_{\mathrm{vis}}$, $\tilde{\boldsymbol{\phi}}^{H}$ and $\tilde{\boldsymbol{\phi}}^{W}$ with the most recent approximation to $\tilde{\mathbf{X}}$ available, yielding in dimensionless variables,

$$\tilde{\mathbf{F}}^{\mathrm{H}} = \iint_{H(t)} \tilde{\boldsymbol{\phi}}^{\mathrm{H}} \, dS, \quad \tilde{\mathbf{M}}^{\mathrm{H}} = \iint_{H(t)} (\tilde{\mathbf{Y}} - \tilde{\mathbf{X}}^{\mathrm{c}}) \wedge \tilde{\boldsymbol{\phi}}^{\mathrm{H}} \, dS_{\mathbf{Y}}, \tag{21}$$

where $\tilde{\mathbf{X}}^{\mathrm{c}}$ is the head centroid. Using also the most recent iterates for $\tilde{\mathbf{U}}^{\mathrm{H}}$ and $\tilde{\mathbf{\Omega}}^{\mathrm{H}}$, the corrections are then given by,

$$\Delta\mathbf{F}^{\mathrm{H}} = \tilde{\mathbf{F}}^{\mathrm{H}} - \mathrm{Sp}^4\left(\frac{\mu}{\xi_\perp}\right)\mathcal{R}^{\mathrm{F}} \cdot \begin{pmatrix} \tilde{\mathbf{U}}^{\mathrm{H}} \\ \tilde{\mathbf{\Omega}}^{\mathrm{H}} \end{pmatrix}, \quad \Delta\boldsymbol{M}^{\mathrm{H}} = \tilde{\mathbf{M}}^{\mathrm{H}} - \mathrm{Sp}^4\left(\frac{\mu}{\xi_\perp}\right)\mathcal{R}^{\mathrm{M}} \cdot \begin{pmatrix} \tilde{\mathbf{U}}^{\mathrm{H}} \\ \tilde{\mathbf{\Omega}}^{\mathrm{H}} \end{pmatrix}. \tag{22}$$

These corrections appear on the right hand side of the linear system.

References

[1] Denissenko P, Kantsler V, Smith DJ, Kirkman-Brown J. Human spermatozoa migration in microchannels reveals boundary-following navigation. Proc Natl Acad Sci USA. 2012;109(21):8007–8010.

[2] Kantsler V, Dunkel J, Polin M, Goldstein RE. Ciliary contact interactions dominate surface scattering of swimming eukaryotes. Proc Natl Acad Sci USA. 2013;110(4):1187–1192.

[3] Gaffney EA, Gadêlha H, Smith DJ, Blake JR, Kirkman-Brown JC. Mammalian sperm motility: observation and theory. Annu Rev Fluid Mech. 2011;43:501–528.

[4] Machin KE. Wave propagation along flagella. J Exp Biol. 1958;35(4):796–806.

[5] Satir P. Studies on cilia: II. Examination of the distal region of the ciliary shaft and the role of the filaments in motility. J Cell Biol. 1965;26(3):805–834.

[6] Brokaw CJ. Bend propagation by a sliding filament model for flagella. J Exp Biol. 1971;55(2):289–304.

[7] Brokaw CJ. Computer simulation of flagellar movement: I. Demonstration of stable bend propagation and bend initiation by the Sliding Filament Model. Biophys J. 1972;12(5):564–586.

[8] Brokaw CJ. Thinking about flagellar oscillation. Cell Motil Cytoskel. 2009;66(8):425–436.

[9] Lindemann CB, Lesich KA. Flagellar and ciliary beating: the proven and the possible. J Cell Sci. 2010;123(4):519–528.

[10] Woolley DM. Flagellar oscillation: a commentary on proposed mechanisms. Biol Rev. 2010;85(3):453–470.

[11] Riedel-Kruse IH, Hilfinger A, Howard J, Jülicher F. How molecular motors shape the flagellar beat. HFSP Journal. 2007;1:192–208.

[12] Lindemann CB. A "Geometric clutch" hypothesis to explain oscillations of the axoneme of cilia and flagella. J Theor Biol. 1994;168(2):175–190.

[13] Hines M, Blum JJ. Bend propagation in flagella. I. Derivation of equations of motion and their simulation. Biophys J. 1978;23(1):41–57.

[14] Camalet S, Jülicher F. Generic aspects of axonemal beating. New J Phys. 2000;2:24.

[15] Brokaw CJ. Computer simulation of flagellar movement VIII: Coordination of dynein by local curvature control can generate helical bending waves. Cell Motil Cytoskel. 2002;53(2):103–124.

[16] Gadêlha H, Gaffney EA, Smith DJ, Kirkman-Brown JC. Nonlinear instability in flagellar dynamics: a novel modulation mechanism in sperm migration? J R Soc Interface. 2010;7:1689–1697.

[17] Tornberg AK, Shelley MJ. Simulating the dynamics and interactions of flexible fibers in Stokes flows. J Comput Phys. 2004;196(1):8–40.

[18] Gueron S, Liron N. Ciliary motion modeling, and dynamic multicilia interactions. Biophys J. 1992;63(4):1045–1058.

[19] Liron N. The LGL (Lighthill–Gueron–Liron) Theorem—historical perspective and critique. Math Meth App Sci. 2001;24(17-18):1533–1540.

[20] Lighthill J. Flagellar hydrodynamics. SIAM Rev. 1976;18(2):161–230.

[21] Mitran SM. Metachronal wave formation in a model of pulmonary cilia. Comput Struct. 2007;85(11):763–774.

[22] Olson SD, Lim S, Cortez R. Modeling the dynamics of an elastic rod with intrinsic curvature and twist using a regularized Stokes formulation. J Comput Phys. 2013;238:169–187.

[23] Rothschild L. Non-random distribution of bull spermatozoa in a drop of sperm suspension. Nature. 1963;198:1221–1222.

[24] Winet H, Bernstein GS, Head J. Observations on the response of human spermatozoa to gravity, boundaries and fluid shear. J Reprod Fertil. 1984;70(2):511–523.

[25] Fauci LJ, McDonald A. Sperm motility in the presence of boundaries. B Math Biol. 1995;57(5):679–699.

[26] Smith DJ, Gaffney EA, Blake JR, Kirkman-Brown JC. Human sperm accumulation near surfaces: a simulation study. J Fluid Mech. 2009;621:289–320.

[27] Elgeti J, Kaupp UB, Gompper G. Hydrodynamics of sperm cells near surfaces. Biophys J. 2010;99(4):1018–1026.

[28] Crowdy D, Samson O. Hydrodynamic bound states of a low-Reynolds-number swimmer near a gap in a wall. J Fluid Mech. 2011 1;667:309–335.

[29] Davis AMJ, Crowdy DG. Stresslet asymptotics for a treadmilling swimmer near a two-dimensional corner: hydrodynamic bound states. Proc R Soc Lond A. 2012;468(2148):3765–3783.

[30] Crowdy DG, Davis AMJ. Stokes flow singularities in a two-dimensional channel: a novel transform approach with application to microswimming. Proc R Soc Lond A. 2013;469(2157):20130198.

[31] Lopez D, Lauga E. Dynamics of swimming bacteria at complex interfaces. Phys Fluids. 2014;26(7):071902.

[32] Pozrikidis C. A practical guide to boundary element methods with the software library BEMLIB. CRC Press; 2010.

[33] Cortez R, Fauci L, Medovikov A. The method of regularized Stokeslets in three dimensions: analysis, validation, and application to helical swimming. Phys Fluids. 2005;17(3):031504.

[34] Smith DJ. A boundary element regularized Stokeslet method applied to cilia-and flagella-driven flow. Proc R Soc Lond A. 2009;465(2112):3605–3626.

[35] Cortez R. The method of regularized Stokeslets. SIAM J Sci Comput. 2001;23:1204–1225.

[36] Gray J, Hancock GJ. The propulsion of sea-urchin spermatozoa. J Exp Biol. 1955;32:802–814.

[37] Pozrikidis C. Boundary integral and singularity methods for linearized viscous flow. Cambridge University Press; 1992.

[38] Gueron S, Levit-Gurevich K. A three–dimensional model for ciliary motion based on the internal 9+2 structure. Proc R Soc Lond B. 2001;268(1467):599–607.

[39] Brokaw CJ. Simulating the effects of fluid viscosity on the behaviour of sperm flagella. Math Meth Appl Sci. 2001;24(17-18):1351–1365.

[40] Goldstein RE, Powers TR, Wiggins CH. Viscous nonlinear dynamics of twist and writhe. Phys Rev Lett. 1998;80(23):5232.

[41] Fornberg B. Generation of finite difference formulas on arbitrarily spaced grids. Math Comput. 1988;51(184):699–706.

[42] Smith DJ, Gaffney EA, Gadêlha H, Kapur N, Kirkman-Brown JC. Bend propagation in the flagella of migrating human sperm, and its modulation by viscosity. Cell Motil Cytoskel. 2009;66:220–236.

[43] Montenegro-Johnson TD, Gadêlha H, Smith DJ. Spermatozoa scattering by a microchannel feature: an elastohydrodynamic model, Supporting Data; 2015. http://dx.doi.org/10.5061/dryad.4767b.

[44] Katz DF, Blake JR, Paveri-Fontana SL. On the movement of slender bodies near plane boundaries at low Reynolds number. J Fluid Mech. 1975;72(3):529–540.

[45] Spagnolie SE, Lauga E. Hydrodynamics of self-propulsion near a boundary: predictions and accuracy of far-field approximations. J Fluid Mech. 2012;700:105–147.

[46] Nguyen H, Ortiz R, Cortez R, Fauci L. The action of waving cylindrical rings in a viscous fluid. J Fluid Mech. 2011;671:574–586.

[47] Cortez M R Nicholas. Slender body theory for Stokes flows with regularized forces. Comms Appl Math Comput Sci. 2012;7(1):33–62.

[48] Elgeti J, Gompper G. Wall accumulation of self-propelled spheres. Eur Phys Lett. 2013;101(4):48003.

[49] Wan KY, Leptos KC, Goldstein RE. Lag, lock, sync, slip: the many 'phases' of coupled flagella. J Roy Soc Int. 2014;11(94):20131160.

[50] Bees MA, Croze OA. Mathematics for streamlined biofuel production from unicellular algae. Biofuels. 2014;5(1):53–65.

[51] Park S, Hwang H, Nam SW, Martinez F, Austin RH, Ryu WS. Enhanced Caenorhabditis elegans locomotion in a structured microfluidic environment. PLoS One. 2008;3(6):e2550.

[52] Majmudar T, Keaveny EE, Zhang J, Shelley MJ. Experiments and theory of undulatory locomotion in a simple structured medium. J R Soc Interface. 2012;9(73):1809–1823.

[53] Dreyfus R, Baudry J, Roper ML, Fermigier M, Stone HA, Bibette J. Microscopic artificial swimmers. Nature. 2005;437(7060):862–865.

[54] Espinosa-Garcia J, Lauga E, Zenit R. Fluid elasticity increases the locomotion of flexible swimmers. Phys Fluids. 2013;25(3):031701.

Short title for page headings: *Scattering of sperm by a microchannel feature*

(a) Problem domain

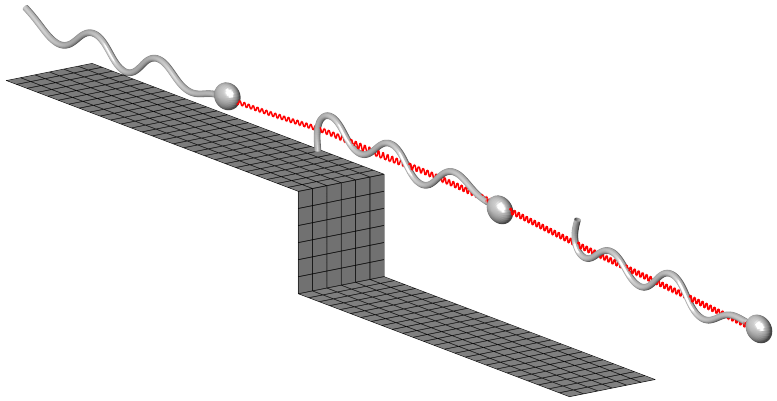

(b) Waveforms in infinite fluid

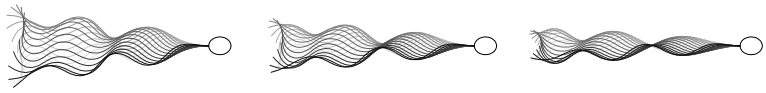

Sp = 13 Sp = 15 Sp = 17

Figure 1: Example results from nonlocal elastohydrodynamic simulation. (a) Plot of the problem domain, including the boundary element meshes for the wall and swimmer, and a plot of the trajectory, computed at Sp = 13. (b) Waveforms in infinite fluid of flagella driven by the same internal force at different sperm numbers. The effect of increasing sperm number is to reduce cell yaw and bending in the proximal end of the flagellum, as is observed in the waveform of sperm in high viscosity medium [42].

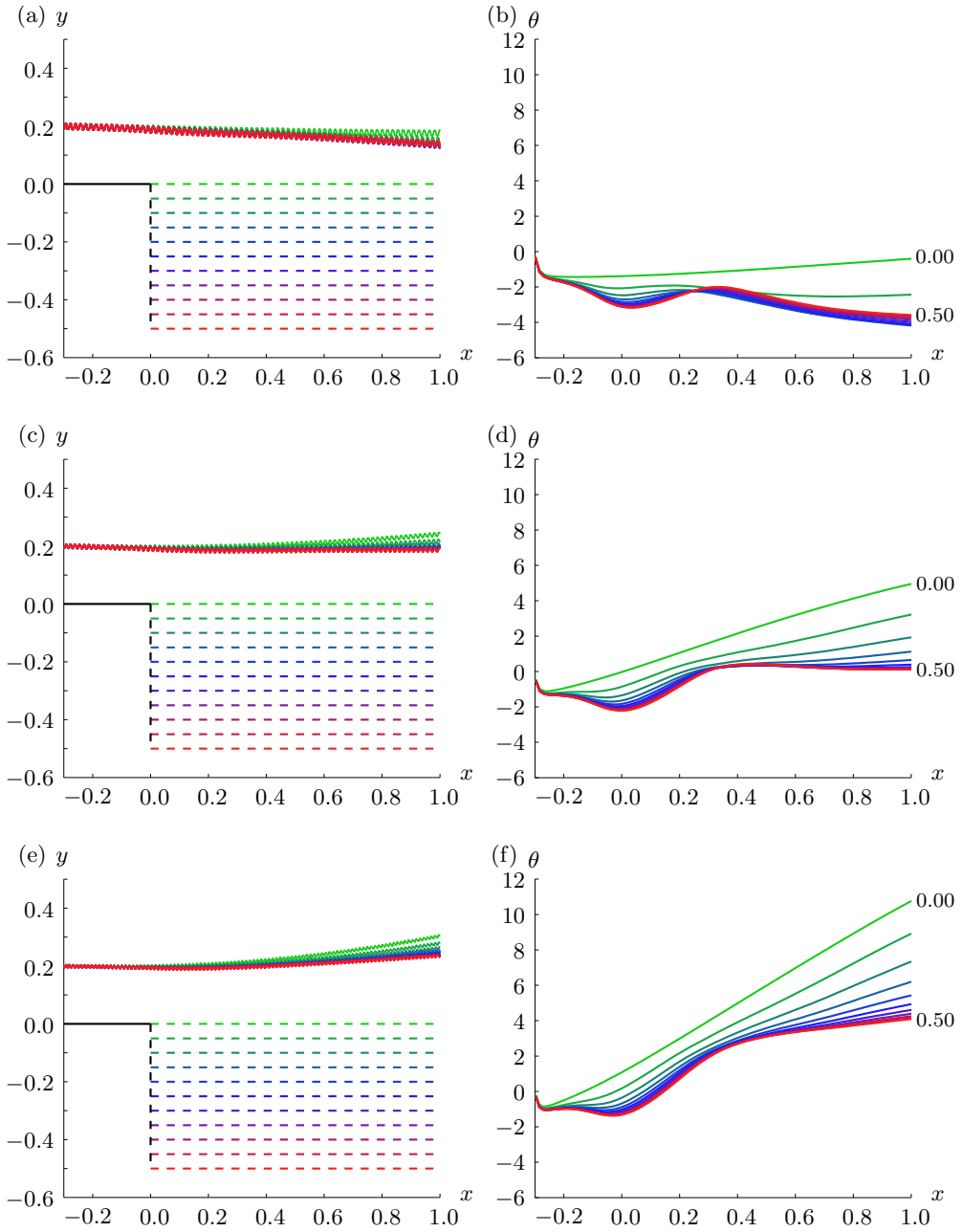

Figure 2: Projected trajectories $(X(0,t), Y(0,t))$ and angles of trajectories $\theta := \arctan dY/dX(s=0)$ for different sperm numbers as a function of changing the height of the backstep. (a, b) Sp = 13, (c, d) Sp = 15, (e, f) Sp = 17. Colour corresponds to the backstep heights shown in (a, c, e).

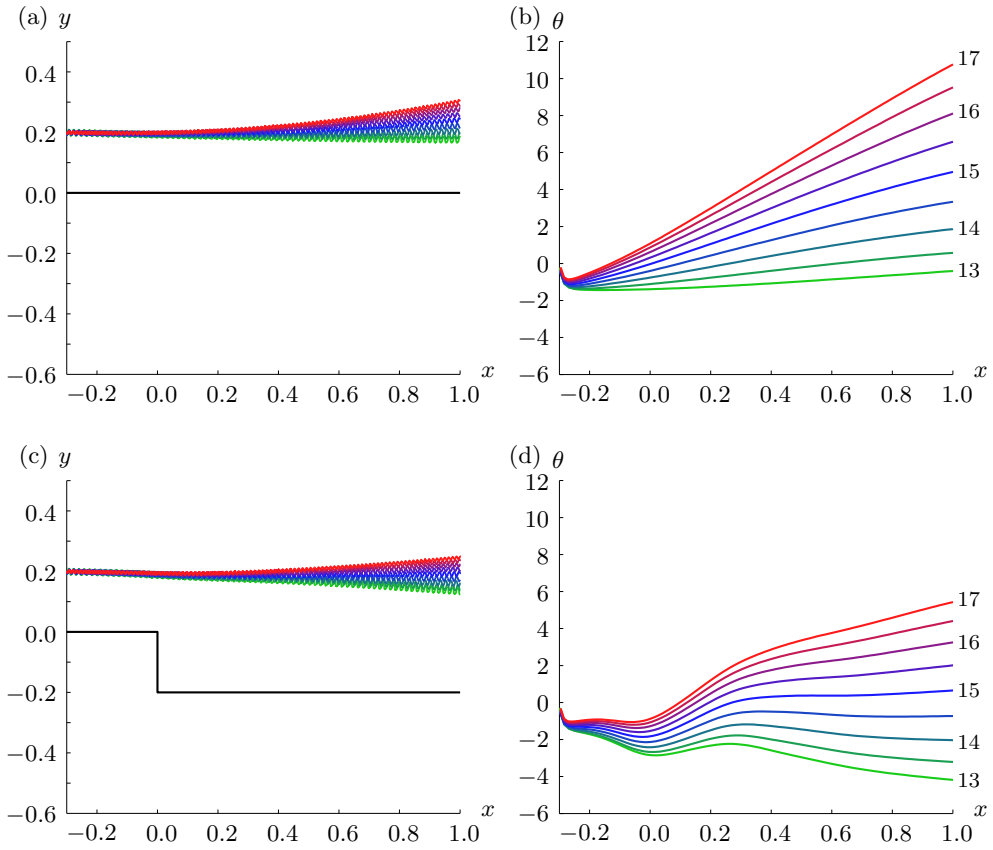

Figure 3: Projected trajectories $(X(0,t), Y(0,t))$ and angles of trajectories $\theta := \arctan dY/dX(s=0)$ for varying sperm number over fixed geometry.(a, b) show trajectories and angles with a 'strip', i.e. zero backstep height, (c, d) with backstep height $0.2L$. Colour is matched to sperm number, light green denoting Sp $= 13$ and red denoting Sp $= 17$, intermediate colours moving in increments of 0.5.

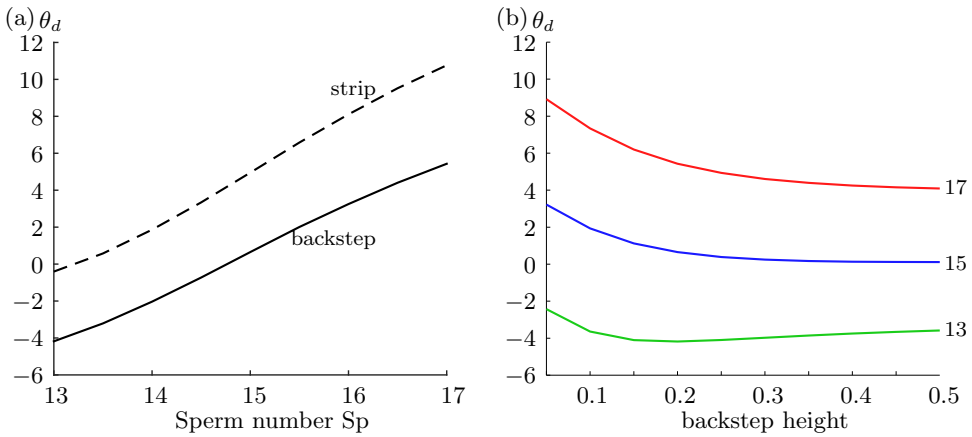

Figure 4: The effect of the backstep on scattering, showing 'final' deflection at $x = 1.0L$, for (a) strip and backstep ($h = 0.2L$) and a range of sperm numbers, (b) Sp $= 13, 15, 17$ and a range of backstep heights. Colour in (b) denotes sperm number as indicated by labels on the right hand side.

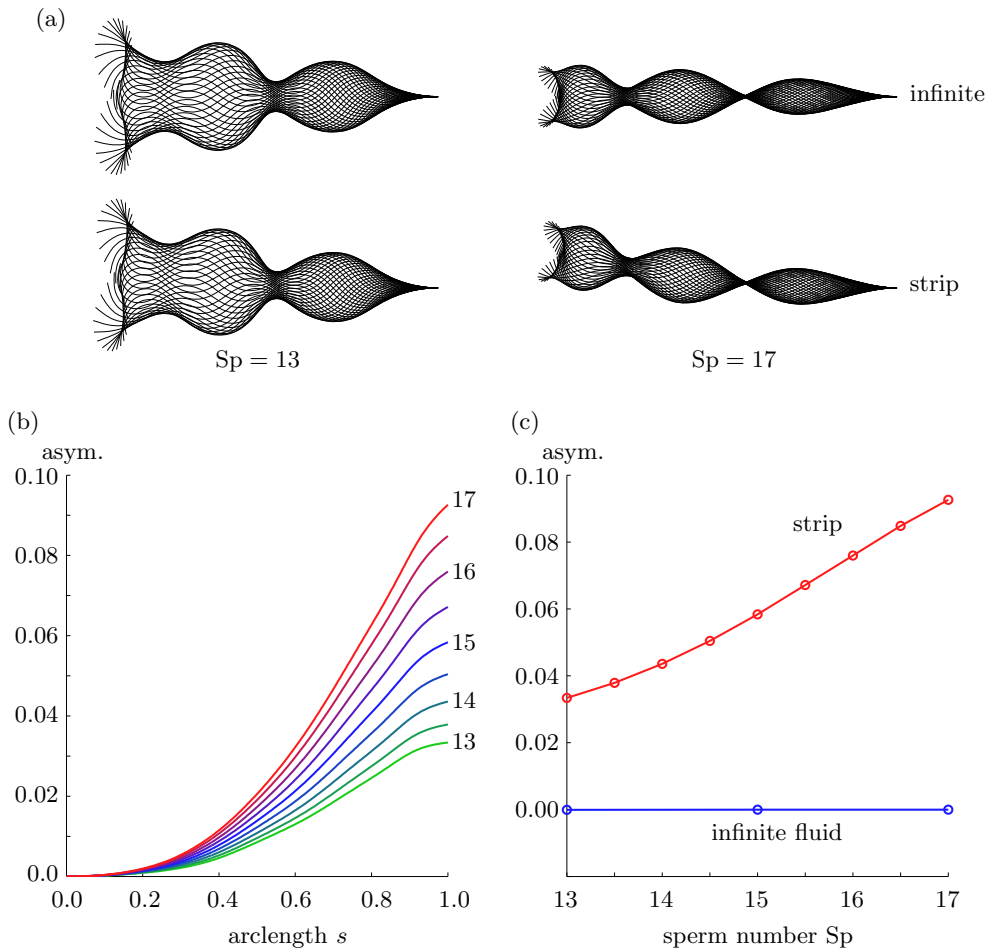

Figure 5: Boundary-induced waveform asymmetry, increasing with sperm number. (a) Symmetric waveforms of sperm flagella swimming in infinite fluid, and asymmetric forms over the boundary strip for Sp = 13 and Sp = 17. (b) Flagellar asymmetry (defined in text) as a function of arclength, for a cell swimming over a strip along the flagellum. Colour in (b) is matched to sperm number, light green denoting Sp = 13 and red denoting Sp = 17, intermediate colours moving in increments of 0.5. (c) Asymmetry at $s = 1$ at the endpoint of the flagellum, as a function of sperm number Sp, showing an increase in asymmetry with sperm number for the strip (red), and negligible asymmetry for the infinite fluid case (blue).